Draft version December 11, 2023
Typeset using LaTeX **preprint** style in AASTeX63

The Hidden Clumps in VY CMa Uncovered by ALMA

Roberta M. Humphreys,[1] A. M. S. Richards,[2] Kris Davidson,[1] A. P. Singh,[3] and
L. M. Ziurys[4]

[1] *Minnesota Institute for Astrophysics, University of Minnesota, Minneapolis, MN 55455, USA*
[2] *Department of Astronomy University of Manchester, UK*
[3] *Department of Chemistry and Biochemistry University of Arizona, USA*
[4] *Department of Astronomy; Department of Chemistry, and Steward Observatory University of Arizona, USA*

(Received; Revised; Accepted)

Submitted to AJ

ABSTRACT

The red hypergiant VY CMa is famous for its very visible record of high mass loss events. Recent CO observations with ALMA revealed three previously unknown large scale outflows (Paper I). In this paper we use the CO maps to investigate the motions of a cluster of four clumps close to the star, not visible in the optical or infrared images. We present their proper motions measured from two epochs of ALMA images and determine the line of sight velocities of the gas in emission at the clumps. We estimate their masses and ages, or time since ejection, and conclude that all four were ejected during VY CMa's active period in the early 20th century. Together with two additional knots observed with HST, VY CMa experienced at least six massive outflows during a 30 year period with a total mass lost ≥ 0.07 $M_{\odot}$. The position-velocity map of the ^{12}CO emission reveals previously unnoticed attributes of the older outer ejecta. In a very narrow range of Doppler velocities, ^{12}CO absorption and emission causes some of this outer material to be quite opaque. At those frequencies the inner structure is hidden and we see only emission from an extended outer region. This fact produces a conspicuous but illusory dark spot if one attemnpts to subtract the continuum in a normal way.

Keywords: Massive Stars; Mass Loss; Circumstellar Matter; VY CMa

1. VY CMA'S MASS LOSS HISTORY AND THE ALMA CLUMPS

Mass loss is observed across the upper HR Diagram and alters the evolution of the most massive stars. It may be slow and continuous or occur in more dramatic high mass loss events which may be irregular or single giant eruptions. In the red and yellow supergiants, these mass loss events may determine their final fate whether as supernovae or direct collapse to the black hole.

Corresponding author: Roberta Humphreys
roberta@umn.edu

The red hypergiant VY CMa is one of the most important evolved massive stars for understanding the role of high mass loss episodes on the final stages of the majority of massive stars which pass through the red supergiant stage. Its mass loss history is highly visible in optical and infrared images with prominent arcs and filaments and clumps of knots throughout its extended diffuse ejecta. Doppler velocities of K I emission, together with proper motions of the discrete ejecta (Humphreys et al. 2005, 2007, 2019) demonstrated that the arcs and clumps of knots are spatially and kinematically distinct from the diffuse ejecta and were expelled in separate events over several hundred years with several episodes in the last century (Humphreys et al. 2021)

New high resolution images with ALMA (Singh et al. 2023), hereafter Paper I, reveal a more extended diffuse ejecta with at least three previously unknown prominent large arcs or outflows observed in CO and HCN emission. The addition of three major outflows expands our record of its high mass loss episodes and frequency, and presents additional challenges to possible models for their origin in VY CMa and similar luminous red supergiants.

ALMA Science Verification sub-mm and continuum emission images of VY CMa at 321, 325 GHZ and 658 GHz (Richards et al. 2014; O'Gorman et al. 2015) earlier revealed an additional, large, potentially massive clump or knot close to the star. It is not visible in the optical HST images. Designated Clump C by Richards et al. (2014), it is optically thick at these frequencies with an estimated dust mass of 2.5×10^{-4} $M_\odot$, or 5×10^{-2} $M_\odot$ assuming a gas to dust ratio of 200. Using the Science verification data for Band 5 at 163 - 211 GHz, Vlemmings et al. (2017) concluded that the dust in Clump C was optically thick even at 178 GHz, and estimated a dust mass of $> 1.3 \times 10^{-3}$ $M_\odot$ or a total mass (dust + gas) of more than 0.1 $M_\odot$. Making it potentially the most massive ejecta in VY CMa.

It is not surprising that Clump C has increased questions about VY CMa's mass loss history and its mass loss mechanism. Using additional ALMA observations in Bands 6 and 7 with a higher angular resolution of $0\farcs1$, Kaminski (2019) identified three additional features or smaller clumps clustered near Clump C and the star. See Figure 3 in Kaminski (2019) and our Figure 1. All are dusty and he comments that the dust mass for Clump C may be even higher than suggested by Vlemmings et al. (2017), but notes that porosity would allow a lower dust mass. For example, with higher resolution ALMA images, Asaki et al. (2020) show that Clump C is resolved into many small condensations with a range of sizes and intensities.

Despite its significance, there is much we don't know about Clump C and associated knots such as their motions, spatial orientation with respect to VY CMa, and when they were ejected. Do they represent a single massive eruption or are they from separate events over a period of time? In this paper we report on the proper motions of Clump C and its neighbors measured from two epochs of continuum images observed with ALMA, and the motions of the CO gas in emission at the clumps. Hereafter, to distinguish them from the numerous knots, clumps etc observed in the optical images we refer to them in this paper as the ALMA clumps.

In the next section we describe our observations and proper motion measurements. In section three we discuss the line of sight velocities of the CO emission at the four ALMA clumps. Section 4 summarizes their total motion, orientation and ages or time since ejection and relation to VY CMa's other recent mass loss events. In section 5, we estimate the masses of the clumps and review the

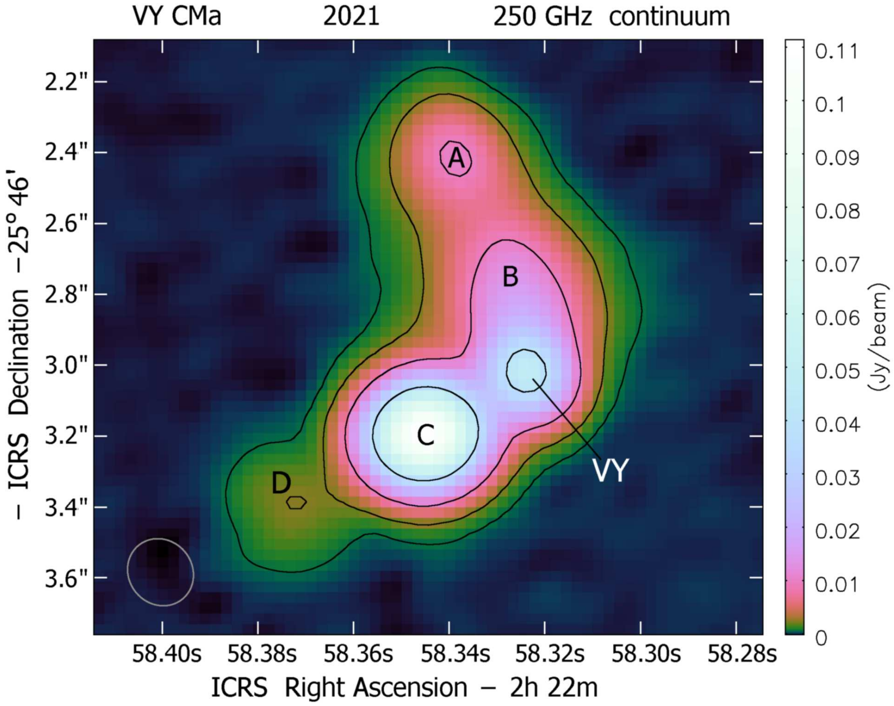

Figure 1. The continuum image at 249 GHz. The contours showing the structure and outlines of the clumps are in multiples of (1, 4, 16, 64) $\times I_1$, where $I_1 \approx 0.6$ mJy/beam $\approx$ 8 mJy arcsec^{-2}. The brightness temperature at the outer contour is about 0.2 K. The synthesized beam (FWHM) is shown as an ellipse in the lower left corner.

energies involved in these high mass loss events. The outer ejecta revealed by the CO emission and its obscuration at Clump C is discussed in Section 6. The final section is a review of questions about VY CMa's evolutionary state.

2. DATA AND PROPER MOTION MEASUREMENTS

Our high resolution observations,[1], obtained with ALMA in Band 6 covering frequencies 216 to 270 GHz are described in Paper I. In this paper we use the continuum image at 249 GHz and the CO image cube with spatial resolution $0\farcs2$ and velocity resolution of 1.25 km s^{-1}. The observational parameters are described in Table A1 in the Appendix. Our continuum image at 249 GHZ is shown in Figure 1. Figure 2 shows the ^{12}**CO emission at the clumps in two representative** channels. The feature labeled B' is an outflow not mentioned in previous papers, and is not present in the continuum images [2] Also Note that the brightest ^{12}CO emission identified with the star is not centered on the position of VY CMa, **and emission to the east dominates in all velocity ranges with bright CO emission**. The peak of the ^{12}CO emission line profile **VY CMa** shown in the Appendix, has a blue shift with respect to the star's expected LSR velocity of 22 km s^{-1}. Thus a cloud of CO gas (and dust) may be asymmetric and probably expanding relative to VY CMa.

[1] **project 2021.1.01054.S**

[2] It is observed in the ^{12}CO data at Doppler velocities $+31 \lesssim V_{LSR} \lesssim +47$ km s^{-1}, but not in the continuum (see Figure 1). Hence we cannot estimate its proper motion. Lacking appreciable continuum emission, most likely it has less mass than A, B, C, or D.

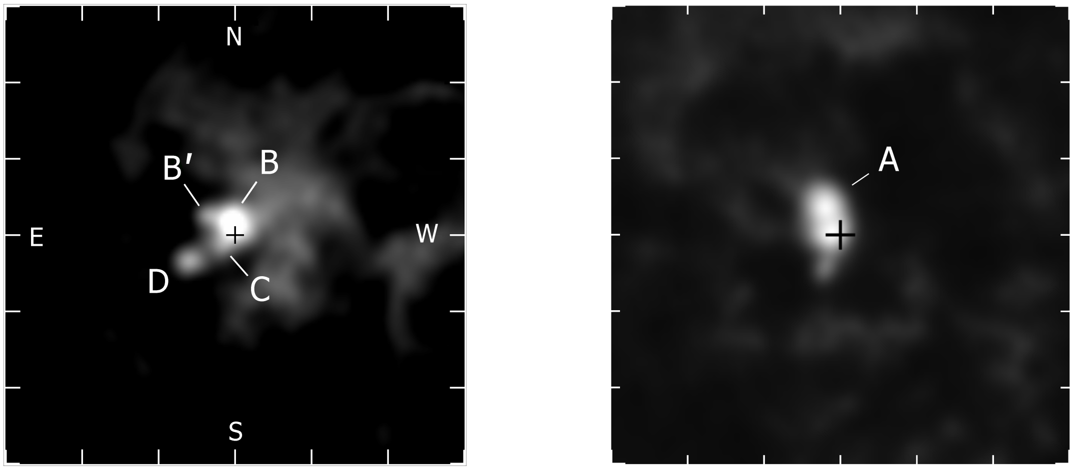

Figure 2. ^{12}CO images of a $6'' \times 6''$ region centered on VY CMa. **The tick marks are** $1''$. Clumps B, C and D are redshifted relative to VY CMa and observed over the same range of Doppler velocities while Clump A is blueshifted. (a) ^{12}CO emission at V_{LSR} 43 km s^{-1} toward Clumps B, C, D, and new outflow B'. (b) toward Clump A at V_{LSR} +6 km s^{-1}. The position of VY CMa is shown as a + in each panel; its Doppler velocity is +22 km s^{-1} relative to the LSR. The brightness scales differ between panels. The images are continuum substracted.

The data reduction steps and calibration are described in Paper I and its Appendix **and summarized in Appendix A in this paper**.

2.1. *Proper Motions of the Clumps*

To measure the proper motion of Clump C and the other knots, we compare their positions relative to VY CMa in our continuum image from 2021 December 09 with an earlier image. The closest dataset to ours in terms of frequency and resolution with a decent time scale is from Kaminski, project 2013.1.00156.S from 2015 September 27 giving a 6.2 yr baseline. The continuum images used for the proper motions, the measurement method, and uncertainties are described in the Appendix.

The separate measurements for 2015 and 2021 are given in Table 1 for the four clumps. Their proper motions, positions, and derived parameters are summarized in Table 2. For example, for Clump C, the continuum images yield separations of 314 mas in 2015 and 341 mas in 2021 with respect to VY CMa. The increase in angular separation of 23 ± 2 mas at a distance of 1.15 kpc[3], is 26.5± 2.8 AU. In 6.2 yrs, the proper motion is 3.7 mas per year and the transverse velocity in the plane of the sky is thus 20.2 ± 2.3 km s^{-1}. The angular change in Declination and Right Ascension between 2015 and 2021 gives the direction of motion (ϕ) for Clump C, 102°, measured N through E. The same parameters are included in Table 2 for the other clumps.

Figure 3 is a map showing the measured proper motions and the direction the clumps are moving. **Clumps C and B have a direction of motion from their proper motions that do not point radially back to the star. The uncertainties in ϕ, the direction of motion in Table 2 however, are within two to three sigma of the position angle for Clumps C and B. Other factors may influence the direction the clumps appear to be moving such as the**

---

[3] the weighted average of Choi et al. (2008)(1.14 (+0.11 -0.09) kpc) and Zhang et al. (2017)(1.20 (+0.13 -0.10) kpc) with a combined uncertainty of ≈ ± 0.08 kpc.

Table 1. Proper Motion Measurements

Date	Object	R.A.	Dec	Total Offset	Date	R.A.	Dec	Total Offset
2015.74	VY CMa	7:22:58.32437	-25:46:3.0687	· · ·	2021.94	7:22:58.32365	-25:46:3.0148	· · ·
”	Clump A	58.33704	2.5366	· · ·	”	58.33817	2.4350	· · ·
	A-VY	0.01267E	0.5321N	· · ·		0.01452E	0.5798N	· · ·
	offset mas	172E mas	532N mas	559±11.8 mas		197E mas	580N mas	612mas±4.1
”	Clump B	58.32545	2.8422	· · ·	”	58.32665	2.7704	· · ·
	B-VY	0.00108E	0.2265N	· · ·		0.00300E	0.2444N	· · ·
	offset mas	15E mas	226N mas	226±8.9 mas		41E mas	244N mas	247±3.4 mas
”	Clump C	58.34395	3.2428	· · ·	”	58.34498	3.1938	· · ·
	C-VY	0.01958E	-0.1741S	· · ·		0.02133E	-0.1790S	· · ·
	offset mas	266E mas	174S mas	318±1.8 mas		290E mas	179S mas	341±0.9 mas
”	Clump D	58.36965	3.4235	· · ·	”	58.37204	3.3897	· · ·
	D- VY	0.04528E	-0.3282S	· · ·		0.04838E	-0.3749S	· · ·
	offset mas	616E mas	328S mas	698±23.3 mas		658E mas	375S mas	757±10.0 mas

Table 2. Measured Positions and Proper Motions

Clump	Proj Dist[a] mas	Pos. Angle degrees	Angular Sep.[b] mas	Proper Motion mas yr^{-1}	Trans. Vel. km s^{-1}	Direct. ϕ degrees
Clump A	560	19	53±12	8.5±2.0	46.3±11.3	27.5 ± 13
Clump B	233	9	21±9.5	3.4±1.5	18.5±8.6	55.3 ± 17
Clump C	320	122	23±2.0	3.7±0.4	20.2±2.3	102.0 ± 5
Clump D	716	120	59±25.3	9.5±4.1	51.8±23.0	138.3 ± 29

[a] The projected distance from VY CMa in mas, is the average of the separation from Kaminski (2019) and for 2015 in Table 1.

[b] The increase in angular sparation or distance from VY CMa from 2015 to 2021.

overall asymmetry of the circumstellar ejecta near VY CMa and the role of magnetic fields, see Section 5.

3. LINE OF SIGHT VELOCITIES TOWARD THE ALMA CLUMPS

At 200 mas resolution, the CO emission in this region is partially resolved into small condensations or features of a size similar to or slightly larger than the beam. Figure 2 shows that Clumps C and B are not well separated from the ^{12}CO emission associated with the star. Clump D, however, appears as a small, nearly circular, emission spot and is spatially separate from the star's ^{12}CO emission in several channels. Clump A is also visible in several blueshifted channels as a relatively bright CO emission spot marginally separate from VY CMa. We find that C and D are optically thick in the continuum but A and B are optically thin (Section 5).

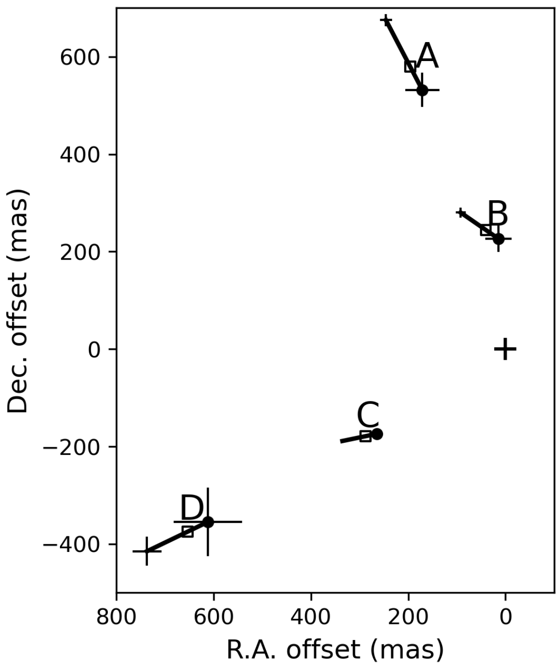

Figure 3. Map of the proper motions showing the direction of motion for the clumps relative to their positions in 2015. The 2015 positions are marked by solid circles and the 2021 positions by hollow squares. The vectors and error bars have been multiplied by three to make them more visible.

Table 3. V_{LSR} Range[a] for the CO Emission Observed at the Clumps

Clump	^{12}CO em	^{13}CO em
	km s^{-1}	km s^{-1}
Clump A	+15 to -4	+15 to -11
Clump B	+33 to +47	+30 to +44
Clump C	+32 to +48	+30 to +44
Clump D	+27 to +48	+26 to +47

[a] VY CMa has V_{LSR} of +22± 1 km s^{-1}.

In Table 3 we summarize the range of Doppler velocities measured toward each clump in the ^{12}CO and ^{13}CO image cubes. The velocities relative to the LSR are measured with respect to their respective rest frequencies. VY CMa has an LSR velocity of 22±1 km s^{-1} based on OH and SiO maser emission from numerous sources. The velocities toward the ALMA clumps demonstrate that clumps C, B and D are redshifted, moving away from and projected behind VY CMa while clump A is blueshifted relative to the star. Kaminski (2019) reported a wider range of velocities from molecular emission from the clumps which can be seen in the line profiles in the Appendix, but Figure 5 discussed below shows that the higher positive and negative velocities are from extended and diffuse separate features.

The CO emission at Clump D appears to be spatially separate from the emission associated with Clump C and the stellar envelope in several channels in the ^{12}CO and ^{13}CO image cubes. **At $\mathbf{V}_{LSR}$ $\lesssim$ +30 km s^{-1}** however, the CO emission peaks for Clump D blend with emission from the star and in velocity with Clump C. Figure 4 shows the summed ^{12}CO image over 28 frequency channels covering the range in V_{LSR} from +49 to +15 km s^{-1}. It clearly shows a continous emission structure to the SE of the star, although the separate channels show that C and D represent different parts of this elongated feature.

In each outflow event there is usually a strong correlation between the Doppler velocity and distance from the star. Hence a position-velocity slice at an oblique angle in the image cube can reveal the local morphology discussed here. Figure 4 illustrates the procedure. The relevant plane in the image cube is defined by position angle 120° which samples both C and D with our spatial resolution. At each frequency channel, we measure the intensity of the signal at positions along a line or slit at $120° \pm 0.05$ arcsec. The extractions for each frequency are stacked. The resulting position-velocity map is shown in Figure 5 for the LSR velocity range -20 to +80 km s^{-1} and reveals the morphology of ^{12}CO emission associated with Clumps D and C and bands of whispy emission or "cirrus" stretching across the lower half and top of the figure. Based on their brightness and size scale the "cirrus" bands represent older ejecta from VY CMa moving at $\approx \pm$ 30 – 40 km s^{-1} **relative to the star**. A prominent emission feature is also visible nearly aligned in position with the brighter star at $\approx$ +30 to +40 km s^{-1}. The dark band at about -3 km s^{-1} that appears to cut off the extended CO emission, is due to optically thick outer ejecta discussed in Section 6.

3.1. *Outflow Velocities of the Clumps*

The diffuse emission feature from V_{LSR} +45 to about +25 km s^{-1} in Figure 5 corresponds to Clump C and D viewed in the different channels in the image cube. Clump C is visible as the bright spot at the top of the arc marked in Figure 5 and based on it position, Clump D is near the tip of the outflow. It is difficult to separate the outflow from the emission associated with VY CMa at LSR velocities less than about +25 km s^{-1}. But, Figure 5 shows an increasing velocity with increasing distance from VY CMa along the arc-like diffuse feature presumably due to an outflow from the star. Thus we suggest that there is an apparent velocity gradient in the ^{12}CO emission towards Clump D with distance from VY CMa.

We use Clump D to examine the kinematics and orientation of the outflow relative to VY CMa. The ^{12}CO emission at Clump D is seen as a small separate emission spots in the image cubes. Figure 6, shows its Doppler velocity relative to the star, V_{rel*}, of the centroid of the ^{12}CO emission in the different channels with the corresponding projected distance from VY CMa. It illustrates what we see in Figure 5, projected onto the plane of the sky. There is a consistent gradient of increasing velocity with increasing distance from the star that is not linear, suggesting an arc-like outflow. .

Together, Figures 5 and 6 demonstrate an outflow of gas probably along an arc, and seen in CO emission toward Clump D, moving away from the star. It may be a remnant of the initial outflow perhaps due to the passage of a shock wave, and appears similar to the K I emission observed behind the leading edges of the large expanding arcs in VY CMa (Humphreys et al. 2005).

Clump D is optically thick **in the continuum (see Section 5)**, so we do not expect to see emission directly behind the clump. Weve already emphasized that Clump D is near the tip of the

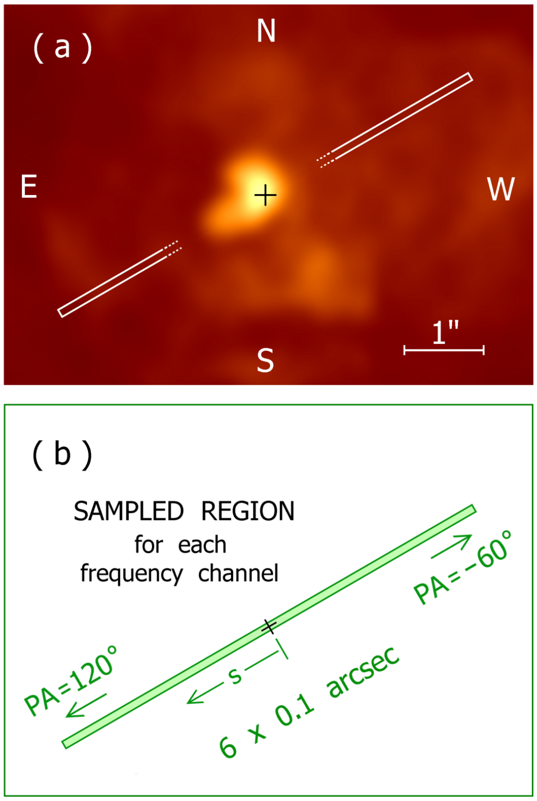

Figure 4. Sketch illustrating how Fig.5 was produced. The upper panel is a sum of the ^{12}CO images at Doppler velocities from +15 to +49 km s^{-1} relative to the LSR, and shows a virtual sampling slit oriented at position angle 120° to include Clumps C and D (Fig. 2). The lower panel shows its spatial parameters. Intensity along that virtual slit was measured for each frequency channel, and the resulting 1-D data sets were stacked to produce the 2-D Fig. 5.

diffuse arc. Figure 6 shows what may be a hook or loop at the very tip of the arc albeit traced by the more diffuse fainter emission. The maximum velocity of CO emission relative to the star is thus approximately 22 km s^{-1}. This velocity coincides with its projected angular distance at $0\farcs73$ in Tables 1 and 2. Consequently, we suggest that this is the Doppler velocity of the ^{12}CO gas at or nearest to Clump D and adopt it for Clump D's line of sight velocity, V_{rel*} with an uncertainty of ± 3 km s^{-1} based on the range in velocities at Clump D's position.

Clump C is also optically thick. It is located at the top of the diffuse arc in Figure 5, near the position of the star at LSR velocities +25 to +30 km s^{-1} and at $\approx 0\farcs4$ from VY CMa corresponding to its position in the continuum image (Table 1). The line profile (Appendix) for Clump C shows a small emission peak at LSR velocity +26 km s^{-1} which we adopt for its line of sight velocity corresponding to +4 km s^{-1}, V_{rel*} with an uncertainty of $\pm approx$ 3 km s^{-1} based on its position in Figure 5 and the width of the emission peak in the line profile.

Clumps A and B are apparently in an outflow extending to the northeast of VY CMa, similar to the diffuse emission arc including Clumps C and D to the southeast (Figure 1). Based on its position angle and projected angular distance from VY CMa, Clump A is very likely associated with the northern extension reported by Richards et al. (2014) and O'Gorman et al. (2015). We observe

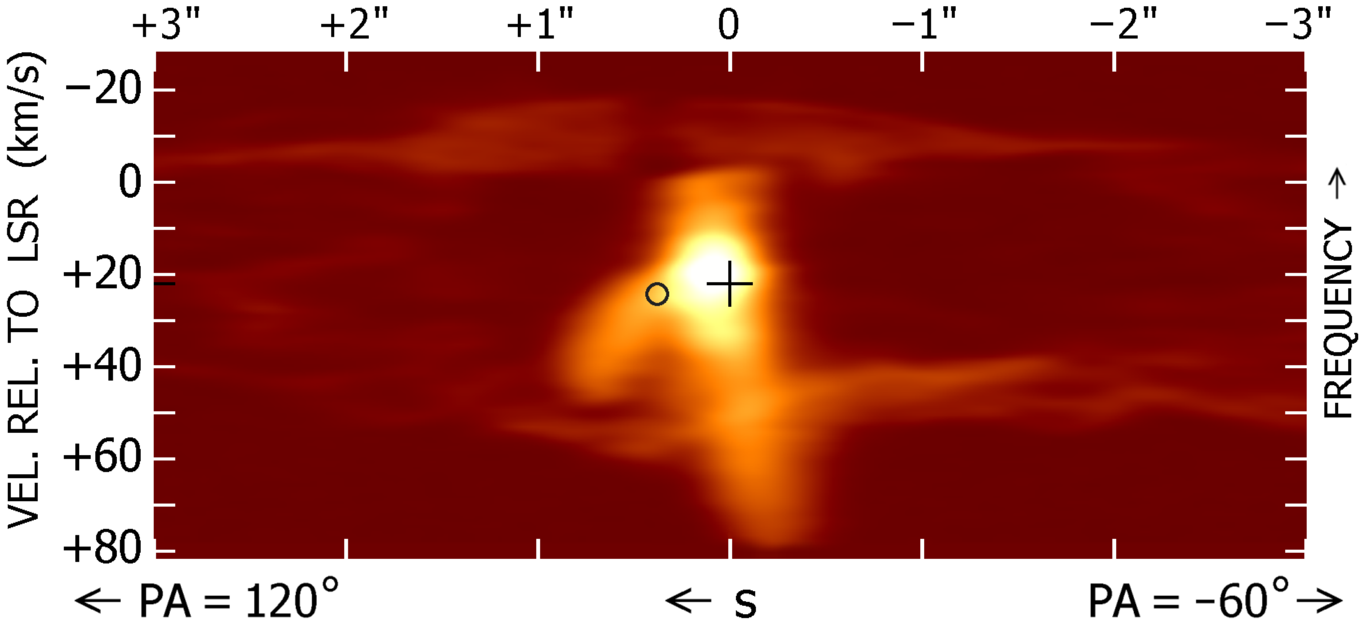

Figure 5. Position-Velocity map of the continuum subtracted ^{12}CO emission at position angle 120°, cf, Fig. 4. The vertical coordinate is the Dopper velocity, while the horizontal scale is the spatial position along a line oriented at position angle 120° (roughly ESE). The location of the star is marked '+, and the approximate postion of Clump C by a small circle. To some extent the Doppler velocities are correlated with location along our line of sight, with the 'near side' at the top of the figure. However, at least two sets of ejecta with different ages and size scales are superimposed, e.g. at velocities +30 to +50 km $^{-1}$. Also see Fig. 8.

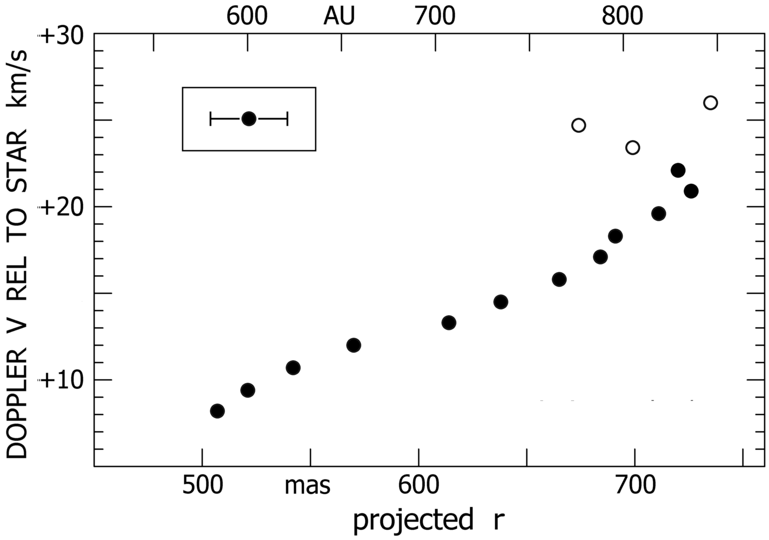

Figure 6. The observed line of sight velocity of the ^{12}CO emission relative to VY CMa toward Clump D vs the corresponding projected distance from the star in mas and AU for 15 channels representing the diffuse arc in Figure 5. The open circles show the less reliable measurements at the end of the arc in Fig. 5. Each measurement used a sampling parameter of 5 pixels (0.″2). The error bar represents the typical uncertainty in the centroid. The main trend agrees with the diffuse arc in Figure 5.

Table 4. Velocities, Distance and Time Since Ejection

Clump	Trans. Vel. km s^{-1}	Doppler Vel.[a] km s^{-1}	Total Vel. km s^{-1}	Orient θ degrees	Dist. AU	Age[b] yrs
Clump A	46.3±11.3	-18±5	49.9±11	-21±7	691±60	66±-12,+19
Clump B	18.5±8.6					69±-19,+26
Clump C	20.2±2.3	+4±3	20.6±3	+11±8	375±30	86±-7,+8
Clump D	51.8±23	+22±3	56.5±21	+23±10	895±90	75±-15,+25

[a] The ^{12}CO line of sight velocity relative to VY CMa, V_{rel*}.

[b] The reference epoch is 2015 for the ages measured from the proper motions and the projected distance from the star in arcsec.

blueshifted CO emission close to the star beginning at LSR Vel +19 km s^{-1} with a position angle of about 25deg which we associate with this outflow. We identify Clump A with the ^{12}CO emission marginally resolved from the star with an LSR velocity range of -4 to +15 km s^{-1}. The blue edge of its emission profile in Figure 10 is cut off by the absorbing ejecta (Section 6) at LSR velocities $\lesssim$ -4 km s^{-1}. The ^{12}CO emission in the image cubes agrees with the position of Clump A for the LSR velocity range $\approx$ +8.6 to -1.6 km s^{-1}. Adopting the middle of this range at +3.5 km s^{-1}, V_{rel*} is -18 ± 5.0 km s^{-1}.

Clump B is more complicated. It is very close to the star (Figure 2) and is not well resolved from the extended emission surrounding the star. It can be seen as an extension on the stellar envelope at redshifted velocities +33 to +47 kms. Its line profile in Figure 10 shows a very broad emission envelope with two peaks on either side of the star's velocity plus a peak near it and the velocity of Clump C. Complications: the redshifted peak may overlap B', and the blueshifted peak overlaps emission from Clump A at the same velocity. . ...

4. MORPHOLOGY AND AGES OF THE ALMA CLUMPS

The velocities are summarized in Table 4 with the total or expansion velocity relative to VY CMa, the orientation or projection angle (θ) with respect to the plane of the sky, the distance from VY CMa corrected for the projection, and an estimate of the age or time since ejection **measured from the proper motions**. The reference epoch for the proper motions, 2015, is the reference date for when the clumps were ejected. The age estimates assume no acceleration or deceleration. We discussed the effect of acceleration or deceleration in Humphreys et al. (2021) and showed that the effect was minimal, on the order of 5% to 10%, less than the errors in the estimated ages.

We find that Clump C is nearly in the plane of the sky as suggested by O'Gorman et al. (2015) and Kaminski (2019). The transverse velocities for Clumps D and A are rather high for knots and condensations close to the star, which have typical velocities of 20 to 30 km s^{-1} (Humphreys et al. 2019, 2021), but both have large uncertainties. These uncertainties from the proper motions dominate the error in the expansion velocity and the age estimates. For reference, the escape velocity for VY CMa, at the stellar surface is $\approx$ 70 km s^{-1} (Humphreys et al. 2021).

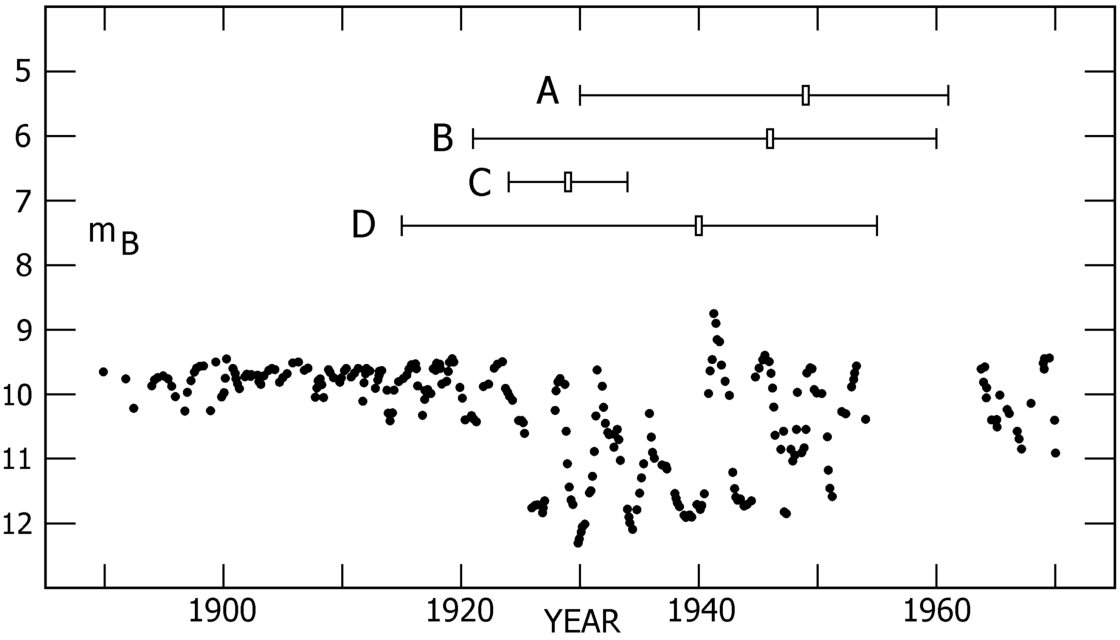

Figure 7. the historic light curve for VY CMa from Robinson (1970) with the estimated ejection dates and possible range of dates from the uncertainty in the expansion velocities for the four clumps.

VY CMa's light curve for the first half of the 20th century is shown in Figure 7 with the probable ejection dates and range. The clumps were all ejected in the early 20th century during VY CMa's very active period 1920 - 1950. There are seven episodes or deep minima during this period each lasting 2 to 3 years which may correspond to the high mass loss events and accompanying obscuration by dust similar to what was observed in Betelgeuse but on a larger scale. Based on the continuum image (Figure 1), it may be tempting to speculate that the four clumps have a common origin in the same high mass loss episode. Within the uncertainties, the clumps could all have been ejected during the same minimum, but this seems unlikely with their different projection angles and directions they are moving.

Figure 1 also shows two major outflows; to the Southeast with Clumps C and D and to the Northeast with Clumps A and B. With their relatively high transverse velocities Clumps D and A may represent the initial ejection and leading edge of a major eruption that in the case of the SE outflow includes Clump C, but their different projections imply different active regions for D and C. Unfortunately we do not have suficinet information to comment on Clump B's association with A or C. Based on their motions, we suggest that Clumps A and C are separate events from C.

The largest and brightest, Clump C with the highest quality measurements, has a relatively well-determined ejection time circa 1930[4]. Although Clump B's spatial orientation is uncertain, Clump C and B have similar proper motions, and velocities with respect to VY CMa. This active period might also correspond with the ejections of knots W1 A and B just to the west of VY CMa (Humphreys et al. 2019). W1-B has an estimated ejection date of circa 1932. If so, their different directions, on opposite

---

[4] Humphreys et al. (2021) estimated a similar ejection time for Clump C adopting the average expansion velocity from the visible knots with the 1999 reference epoch. Kaminski (2019) showed the same light curve but adopting a higher velocity initially concluded that the clumps did not correspond with the minima.

Table 5. Derived Parameters for the ALMA Clumps

Clump	Flux Density[a]	Brightness Temp[b]	Dust Temp	Opt. Depth	Dust Mass	Total Mass $M_\odot$
	mJy	degrees K	degrees K	τ	$M_\odot$	dust + gas
Clump A	22	11	352	0.03	$\approx 8\times 10^{-5}$	$\approx 1.6\times 10^{-2}$
Clump B	33	11				
Clump C	161	243	478	0.71	$> 1.2\times 10^{-4}$	$> 2.4\times 10^{-2}$
Clump D	5	186	305	0.94	$> 3\times 10^{-5}$	$> 6\times 10^{-3}$

[a] Continuum emission at 249 GHz, mostly thermal emission by dust grains.

[b] Based on the continuum flux density and apparent projected size of each clump (FWHM). May be under estimated because the clumps are not well resolved.

sides of VY CMa, would be evidence that surface activity may occur over much of the star during the same short period yielding separate outflows.

Six outflows or ejecta are now identified within VY CMa's $\approx$ 25 year active period beginning about 100 years ago. Seven minima are observed, thus there were very likely additional ejecta which are obscured or occurred out of our current line of sight. In the next section we discuss the mass lost in these ejections and the energy required.

5. MASS LOST AND THE MASS LOSS MECHANISM IN VY CMA

Measured and derived parameters including the integrated flux density at 249 GHz and the dust mass for each clump are summarized in Table 5. The expected grain or dust temperature, T_{gr}, is **estimated using the standard approximation $T_{gr} \approx \zeta\,(R_*/r_{gr})^{1/2}\,T_*$, where the efficiency factor ζ is close to unity for most normal types of grains above $T_{gr} \sim 200$ K (see, e.g., Draine (2011)). r_{gr} is the distance of the clump from the star corrected for the projection angle in Table 4, with an adopted temperature of 3500 K (Wittkowski et al. 2012) for VY CMa and radius, R_*, $\approx$ 7 AU. A more precise approximation requires information that is not readily available. This approximation assumes that the dust is optically thin**. The optical depth τ is estimated from the standard relation between the observed and dust temperatures. We determined the dust mass following O'Gorman et al. (2015) with the same input parameters and with an adopted gas to dust ratio of 200 (Mauron & Josselin 2011) for the total mass lost. The mass estimates, especially for Clumps C and D, are lower bounds since the calculation uses the dust temperature for an optically thin case.

Clumps C and A have our highest mass estimates. Our result for Clump C is comparable to that from O'Gorman et al. (2015), but is less than the value from Vlemmings et al. (2017). The masses for the other two clumps are typical for other knots in VY CMa with dust masses based primarily on their infrared fluxes, see Table 1 in Humphreys & Jones (2022). Clumps C and A may be representative of the more massive outflows or ejecta in VY CMa. The energies required though is quite modest for VYCMa with a luminosity of 3×10^5 $L_\odot$. For example, Clump C's kinetic energy is a little more than 10^{44} ergs, assuming its outflow velocity of 21 km s^{-1}, equivalent to VY CMa's luminosity in less than a day.

The total mass shed during this active period by the four ALMA knots is ≥ 0.05 $M_\odot$. Assuming 10^{-2} $M_\odot$ for Knots W1 A and B, the estimated mass lost from observed ejecta is at least 0.07 $M_\odot$ yielding an effective mass loss rate of $\approx 10^{-3}$ $M_\odot$ yr^{-1} or more in 25 to 30 yrs. The mass lost in these discrete episodes not only dominates VY CMa's recent mass loss history (Humphreys et al. 2021; Humphreys & Jones 2022), but explains its measured high mass loss rate of 4 to 6 $\times$ 10^{-4} $M_\odot$ yr^{-1} (Danchi et al. 1994; Shenoy et al. 2016). The mass loss estimate from the recent dimming of Betelgeuse (Montargès et al. 2021) together with the mass in its circumstellar condensations (Kervella et al. 2009, 2011), also contribute significantly to its measured mass loss rates (Humphreys & Jones 2022). Betelgeuse and the similar recent dimming of the high luminosity K-type supergiant RW Cep (Jones et al 2023; Anugu et al 2023) are increasing evidence that high mass surface outflows are more common in RSGs and a major contributor to their mass loss.

The primary questions concern the mass loss mechanism for the high mass loss episodes. The standard methods for mass loss that work well for red giants and AGB stars, e.g. radiation pressure on grains, pulsation and convection, are not adequate for RSGs and cannot account for the elevation of the material to the dust formation zones (Arroyo-Torres et al. 2013, 2015; Climent et al. 2020) in the very dusty, high luminosity RSGs like VY CMa.

The dynamical timescale for VY CMa is about three years, comparable to the timescales for a non-radial instability or a magnetic/convective event similar to Coronal Mass Ejections (CME). The presence of magnetic fields is supported by the circular polarization and Zeeman effect observed in the OH, H_2O, and SiO masers in its ejecta (Vlemmings et al. 2002; Richter et al. 2016; Vlemmings et al. 2017). Vlemmings et al. (2017) reported polarized dust emission from magnetically aligned grains on sub-arcsec scales close to the star. Humphreys & Jones (2022) estimated a surface field of 500G based on the magnetic field strengths from the maser emission in the ejecta. They also showed that scaling the most energetic Solar CME's to the kinetic energies of the knots in VY CMa, would require a 1000 G field similar to the above estimate.

Fundamental clues to VY CMa's mass loss can be seen in the morphology of its ejecta. In this regard, stellar outflows can be categorized by their acceleration mechanisms: (1) Supernova outflows are driven by blast waves. They generally produce numerous filaments, often with roughly spheroidal symmetry. Nova remnants may also fit into this category. (2) Giant eruptions are driven by continuum radiation pressure (Davidson 2020). The only well-resolved example, η Car, exhibits fossil turbulence cells that visually resemble volcano eruptions and some other terrestrial-scale explosions. (3) Planetary nebulae are driven by dynamical instabilities. Their filamentary systems often include small mass condensations and large-scale bipolar or multipolar symmetries. (4) Solar or stellar activity is driven by interactions of convection and plasma physics with magnetic fields. The outbursts are spatially localized rather than global, with loops and arcs.

The morphology of VY CMa's ejecta is most similar to stellar activity. A lack of global symmetry is obvious, and each loop or arc (see Humphreys et al. (2005, 2007) and Fig. 9 below) may be a fossilized remnant of initial magnetic confinement of outflowing material. The same process may also create localized mass concentrations like the knots or clumps. The major question is whether MHD-like processes can liberate enough energy for the outburst, in addition to confining it.

6. UNEXPECTED PHENOMENA IN THE OUTER EJECTA

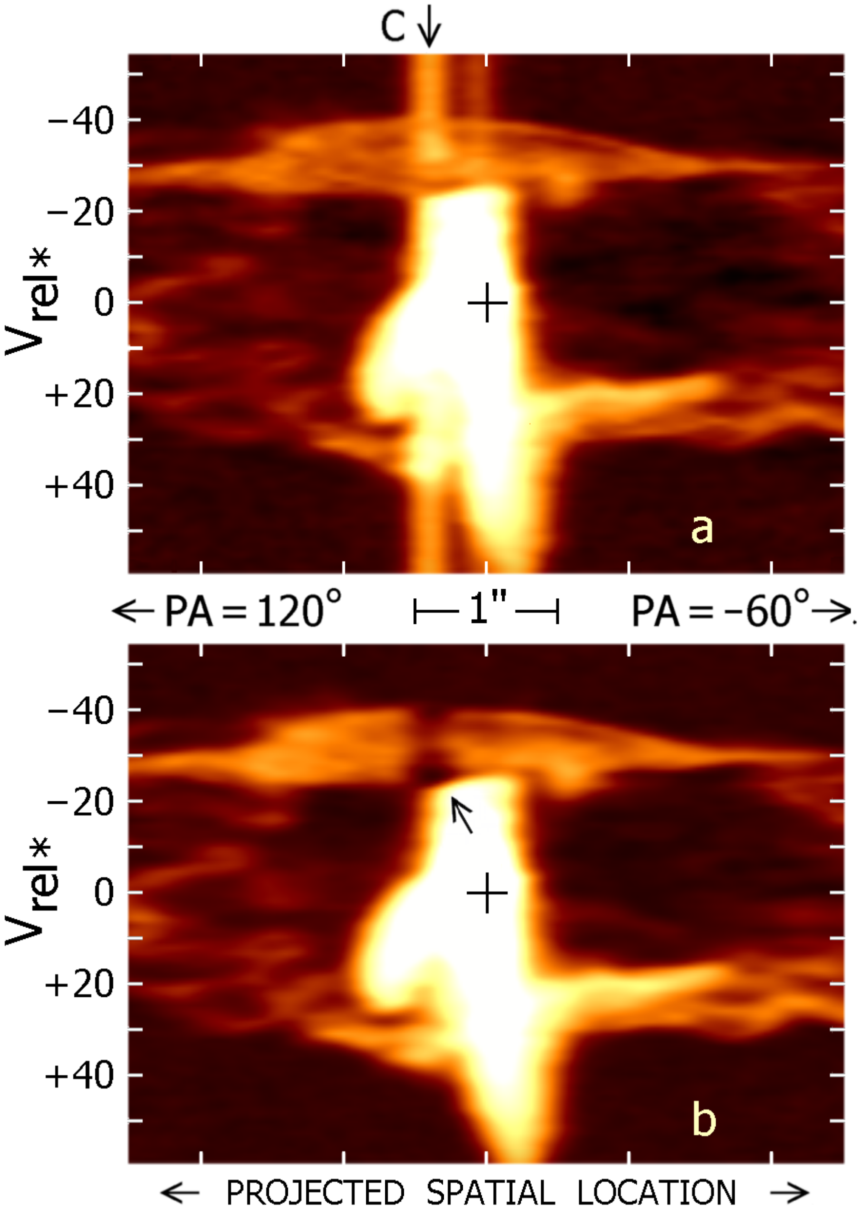

Figure 8. An oblique plane in the image cube, similar to Figure 5. The vertical scale is frequency, represented by the ^{12}CO Doppler velocity relative to the star. The horizontal axis is spatial position along a projected line oriented at position angle 120°, cf. Fig. 4. The star's position is marked by '+'. (a) Total observed intensity, ^{12}CO emission plus continuum. The prominent vertical line just left of center is continuum emission from Clump C. (b) Same image after the formal continuum subtraction process. An arrow marks the invalid dark spot shown in Figure 9 and explained in the text.

Figure 5 in Section 3 was designed to illustrate the Clump C–D structure, but it also reveals remarkable larger-scale details that were not recognized earlier.

Figure 8 is similar to Fig. 5, but has brightness and contrast parameters that show the outer ejecta more clearly. Again the horizontal scale represents projected spatial location along a line with position angle 120° and −60° (roughly ESE and WNW), centered at the star. The vertical scale is frequency expressed as ^{12}CO Doppler velocity relative to the star – e.g., negative velocities at the top of the figure represent ejecta moving toward us.

Unlike most other figures in this paper, Fig. 8a includes the total observed ^{12}CO emission plus continuum; continuum has not been subtracted. Clump C, the strongest continuum source, produces a conspicuous vertical feature about 0.4 arcsec to the left of the star. The bright vertical structure near the center of the figure is mostly ^{12}CO emission in the inner material with $r < 600$ AU, ejected less than 200 years ago. Horizontal cirrus-like features around $V_{rel*} \sim \pm 30$ km s^{-1}, on the other hand, represent older ejecta at $r \sim 3000$ to 8000 AU, with ages $\gtrsim 800$ y. This molecular emission was reported earlier by Ziurys et al. (2007) and in Paper I, while Shenoy et al. (2016) described IR emission from the associated dust. ^{12}CO images at various frequencies confirm that the pattern of inner- vs. outer ejecta is broadly similar toward other position angles.

The upper half of Fig. 8a reveals a fact that was not recognized earlier: the outer ejecta are opaque in a very narrow range of frequencies corresponding to ^{12}CO $V_{rel*} \approx -28$ km s^{-1}. Pictorially the cirrus-like layer forms a conspicuous ceiling to the inner-ejecta emission, and the latter is undetectable in several of the frequency channels. At those frequencies the outer material is optically thick, with brightness temperatures in the range 20–40 K along the lines of sight that we discuss here. This is remarkable, and arguably surprising, for several reasons. (1) In most cases of old, strongly inhomogeneous stellar ejecta, some radiation escapes through interstices or gaps between the filaments or condensations even if each condensation is optically thick. But that is evidently untrue here. (2) The transition is remarkably abrupt in frequency space; for instance, continuum from Clump C is detectable at $V_{rel*} = -22$ km s^{-1} but undetectable at -25 km s^{-1}. (3) The velocity range of opaque material is only about 8 km s^{-1}, even though the outer ejecta are extremely non-spherical. We cannot explore the physical implications of a fully-opaque molecular shell here, because that is beyond the scope of this paper. At present the main point is that one must be aware that it affects our view of the inner ejecta.

Moreover, this case provides a dramatic example of a strange illusion generated by the standard data reduction **described in Paper I and here in Appendix A**. Thoughout this paper, we have attempted to remove the continuum emission in order to focus on ^{12}CO emission. Generally a renormalized 249 GHz continuum image (Fig. 1) is subtracted from the data image for each frequency channel. This procedure is satisfactory at frequencies where the intervening material is transparent. However, it becomes invalid near $V_{rel*} \approx -28$ km s^{-1} because the inner continuum sources are entirely hidden at those frequencies by ^{12}CO absorption and emission in the outer ejecta as described above. Moreover, Clump C dominates in the subtracted continuum image. Figure 9 shows the peculiar result. Figure 9a, like 8a, represents the total observed data without continuum subtraction; it is almost entirely ^{12}CO emission with $T_b \sim 30$ K produced in the opaque layer, with no perceptible contribution by Clump C. Figure 9b is the image after continuum subtraction; it shows a very conspicuous dark spot which is merely a negative image of Clump C. Kaminski (2019) assumed that this is a real feature, which would require strange attributes (e.g., a mismatch between size and internal velocity dispersion). In fact, as stated above, it is an artifact caused by unsuitable continuum subtraction. It can also be seen in Figure 8b, marked by an arrow.

7. COMMENTS ON THE EVOLUTIONARY STATE OF VY CMA

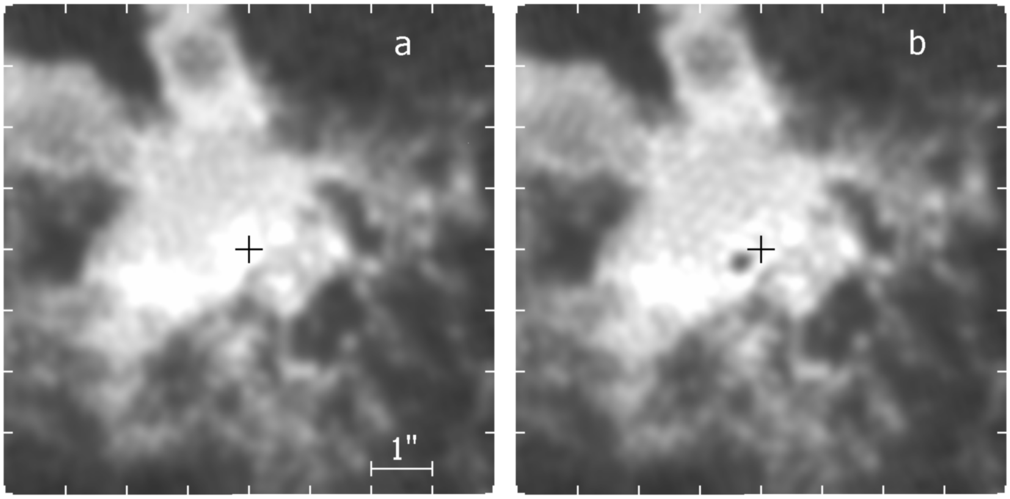

Figure 9. ^{12}CO spatial images at Doppler velocity V_{rel*} -27 km s^{-1}. At this frequency the outer ejecta are optically thick, hiding the inner ejecta. (a) Observed intensity, almost entirely ^{12}CO emission. (b) Result of the formal continuum subtraction procedure which is valid at most other frequencies. The prominent central dark spot is an illusory negative image of continuum from Clump C. In both images, the mottled mesh pattern is an artifact of the interferometry reduction process.

VY CMa's observed properties suggest a very evolved red supergiant that may be near the end of the RSG stage. It is one of most luminous known RSGs with a corresponding initial mass of $\approx$ 30 to 35 M$_\odot$, significantly above the 18M$_\odot$ upper mass for the progenitors of the Type IIP supernovae (Smartt 2015). Thus its final fate may be to either directly collapse to a black hole or evolve back to warmer temperatures before the terminal explosion. Stellar structure models (Eggenberger et al. 2021) show that the latter requires sufficient mass loss to increase the ratio of the He/C core relative to the total mass to send the star on a "blue loop" across the H-R Diagram.

Our observations of the CO emission from the outer ejecta discussed in the previous section, reveal diffuse filamentary ejecta expanding at 30 to 40 km s^{-1} relative to the star at distances of 5 to 6$''$ from VY CMa (Ziurys et al. 2007; Singh et al. 2023). At about 7000 AU from the star, the expansion age of the outflow is 800 to 1100 years. The CO emission appears to surround the more complex inner ejecta including the large arcs in the HST images. The prominent Arc 1 is the oldest with an expansion age of about 800 years (Humphreys et al. 2007). In an independent study based on a radiative transfer model of the CO emission, Decin et al. (2006) concluded that a high mass loss phase in VY CMa began about 1100 years ago. Furthermore, the 37μm image of the cold dust (Shenoy et al. 2016) shows that there is no cold dust beyond a radius of 10$''$, corresponding to an ejection age of about 1400 years. We thus conclude that VY CMa entered its presently observed active phase with relatively frequent massive outflows about 1200 years ago.

We have no explanation for the onset of its enhanced surface activity which may have been stimulated by a change in the interior or more likely a change in the structure of the convective layers. Of course, VY CMa is not alone. Surface outflows have been observed in Betelgeuse and RW Cep, although the record for VY CMa is remakable.

VY CMa also has a unique rich and peculiar chemistry. Twenty-five molecules have been identified in its ejecta including molecules of carbon and silicon. The only comparable star, is the similar luminous RSG, NML Cyg (Singh et al. 2022) with 21 molecules in common with VY CMa. In Paper I, we reported on preliminary $^{12}C/^{13}C$ ratios of 22 to 38 in various structures in the ejecta These ratios are significantly higher than measured in oxygen-rich red giants and supergiants and may be indicators of additional dredge-up perhaps related to VY CMa's surface activity. Our future work will include abundance measurements of the additional molecules observed in the program (Paper I). Their association with separate outflows, arcs, and clumps at different locations and with expansion ages may provide more clues to VY CMa's current state and fate. Another possibility, not often discusssed, is whether VY CMa may be a second generation red supergiant. Similar to lower mass stars, it may have evolved back to warmer temperatures, has now returned and is in a very short high mass loss state prior to core collapse to a black hole.

APPENDIX

A. PARAMETERS FOR THE 2021 ALMA OBSERVATIONS

The parameters for the continuumm and CO images used in this paper are summarized in Table A1. The beam properties are the major and minor axes and position angle. The rms noise $\sigma_{\rm rms}$ is measured within the region of full sensitivity but away from bright emission. The MRS is the maximum recoverable scale of emission which can be imaged accurately. Both cubes were made to cover 36" on a side, out to < 0.3 of the full primary beam sensitivity.

The 2021 data are from the observations described in Paper I, (covering a larger range of frequencies and angular scales). We started from the data delivered from the ALMA Science Archive with all instrumental calibration as well as bandpass, flux scale and phase referencing corrections applied. We split out the VY CMa data, which were adjusted to constant velocity in the VLSR convention in the direction of VYCMa. For each tuning and array configuration, we selected the line-free channels to use these for phase and then amplitude self-calibration. We applied the calibration to all channels. The resolution of the more extended-configuration data varies slightly between tunings and we chose the highest-resolution continuum image for this analysis. For each spectral window, the line-free continuum was substracted from the calibrated visibility data using a first-order linear fit for the image cubes. The image cubes were also made from the unsubtracted data, using the same parameters, for the 12CO, 13CO and HCN lines. The 2015 data are described by Kaminski (2019).

B. THE FITTING METHOD FOR THE PROPER MOTION MEASUREMENTS FOR THE FOUR CLUMPS

The 2021 continuum image (Paper I) used for measuring the proper motion has resolution $0\farcs20 \times 0\farcs18$, rms 0.04 mJy, central frequency 249.34 GHz. The absolute astrometry for the 2015 data (Kaminski 2019) may be worse as at that time antenna positions were less well-determined but our comparison uses only relative positions. The 2015 continuum image used for measuring proper motions has resolution $0\farcs17 \times 0\farcs13$, rms 0.1 mJy, central frequency 230.31 GHz.

Table A1. Characteristics of the Continuum Images and J=2-1 CO Image Cubes

Transition	Date	Center ν	No. chan	Chan. width	$\mathrm{V_{LSR-min}}$ to $\mathrm{V_{LSR-max}}$	MRS	Restoring beam	σ_{rms}
	yyyymmdd	GHz		km s^{-1}	km s^{-1}	arcsec	mas×mas deg	mJy
Continuum	20150927	230.314	–	–	–	1”.6	175×132 70°	0.1
Continuum	20211209	249.339	–	–	–	3”.4	196×180 39°	0.05
^{13}CO	20211216	220.379	144	1.33	–68.58 to +121.38	3”.4	257×241 11°	1.0
^{12}CO	20211216	230.513	158	1.27	–58.74 to +140.63	3”.4	265×251 11°	0.9

We used the CASA task imfit for fitting the continuum peaks of the four Clumps A, B, C and D plus VY CMa, see Figure 1. We treated both the 2015 and 2021 data similarly to ensure comparability. Estimates were first made of the individual peak positions and flux densities using the CASA viewer. 2D Gaussian compoments were then fit to all five peaks simultaneously, using input estimates for the peak flux densities, positions, angular sizes and position angles. The estimates were refined iteratively to reduce the residuals. The residual after fitting to the star only was used to confirm the initial position estimate for B. As the accuracy improved, the peak flux estimates were fixed (starting with the brightest components), leaving the positions and sizes (and thus integrated fluxes) as free parameters. For the 2015 data, once good (stable) position estimates had been obtained for the brightest components these also were fixed in order to avoid the weaker components having unphysically large sizes. Simultaneous fitting should ensure that all the peaks are fit with comparable accuracy and minimise leakage or conversely over-subtraction between components. The relative position uncertainties given in Table 1 due to phase noise are approximately (synthesised beam)/(S/N), for moderately extended array configurations (ALMA memo 620). We adopt the same errors in both coordinates as the synthesised beams are close to circular and have a small elongation, at intermediate angles. These were propagated for the measurements in Table 2.

An additional source of uncertainty arises because the distributions of emission for clumps A, B, C and D are not necessarily Gaussian, and they may have sub-structure which evolves in brightness during the outflow. The apparent fitted, deconvolved sizes varied between 2 synthesised beams and being unresolved but we do not consider the Gaussian approximations good enough to analyse the sizes. We did check as described that in all cases apparent radii of adjacent clumps were significantly less than half the angular separation, so any potential overlap is at too low a level to bias the fit significantly.

After subtracting the fits images, the residual images have rms 0.4 and 0.2 mJy for the 2015 and 2021 data, respectively. The relative position uncertainties due to phase noise are approximately (synthesised beam)/(S/N), for moderately extended array configurations (ALMA memo 620). We adopt the same errors in both coordinates as the synthesised beams are close to circular and elongated at intermediate angles. Positions in Table 1 are given to an extra decimal place to avoid rounding errors in calculating offsets.

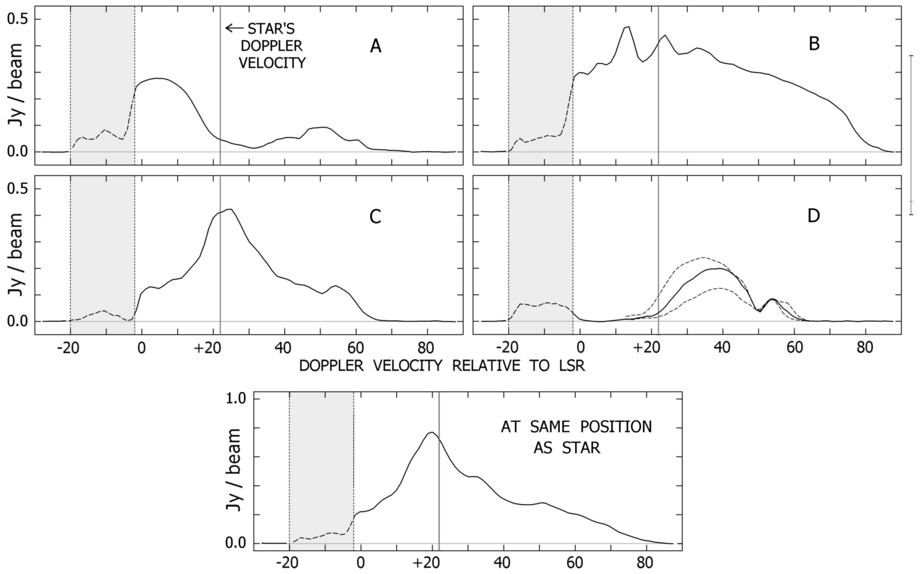

Figure 10. The continuum subtracted ^{12}CO line profiles at the projected centers of Clumps A, B, C, and D with a 1 pixel circular aperture. In the range -20 to -2 km s$^{(}-1)$ near the left side, observed intensities represent an opaque outlying shell which conceals the inner ejecta (Figure 8 and Section 6). As explained in the text, two dashed curves represent locations 100 mas NW and SE of Clump Dś center (NW is brighter, cf. Figure 5). A fifth panel shows intensity along the line of sight to the star, but this emission arises primarily in circumstellar ejecta rather than the star.

C. THE LINE PROFILES FOR THE FOUR CLUMPS AND VY CMA

The clumps' Doppler velocities are difficult to measure, because unrelated emission occurs along and near each line of sight. Fortunately, due to geometrical details, this uncertainty scarcely affects the most important values in Table 4. For example, suppose that Clump D's radial velocity has an unexpectedly large error of 5 km s−1 (cf. Figure 6); this would alter V_{tot} and r by less than 4%, and would change θ by less than 5°. Doppler velocities were not used for the ejection times (Section 4).

Figure 10 shows velocity profiles along lines of sight through Clumps A, B, C, D, and the central star. Gaussian statistics cannot be applied to errors in the velocities of local peaks, because they are dominated by complex systematic effects. For each measurement one must inspect the spatial image for each frequency channel, because some features in Figure 10 represent outer parts of unrelated nearby emission peaks. Error values quoted for Doppler velocities in Table 4 represent, informally, a confidence level roughly equivalent to σ used in formal statistics. If no additional information is available, the realistic uncertainty of a peak location in these data tends to be roughly ±FWHM/4. A more elaborate analysis is not needed, because even the worst credible Doppler velocity errors would not greatly affect V_{tot} and other essential quantities (see above).

Each clump A, B, C, D has individual characteristics. For instance, Figure 10 shows that one wing of Clump A's line profile ($\lesssim -2$ km s^{-1}) is concealed by the opaque shell of outer material described in Section 6. Hence we used only a small velocity interval to estimate its peak. For Clump B, we must decide which local peak is relevant.

Clump D represents the outer terminus of an elongated structure (Figures 4–6), not the center of an isolated feature. Hence the limited spatial resolution has an asymmetric effect: the line profile is contaminated by lower-velocity material to the northwest, while there is much less compensating higher-velocity emission within the p.s.f. This fact is indicated by two dashed curves in Figure 10, showing the profiles at distances of 100 mas in opposite directions from the adopted center of D – specifically, toward position angles −56° and 124°, roughly aligned with the C–D feature (Figure 4). Due to this asymmetric contamination, the peak of D's profile in Figure 10 is several km s^{-1} lower than the Doppler velocity listed in Table 4.

In these circumstances, we measured the C–D feature as a set of spatial positions at well-defined Doppler velocities, rather than velocities at given positions. Figure 6 shows results along that structure. Most of the points fall along a curve that is surprisingly smooth, considering that the measurement process was entirely objective. (A specific peak-location algorithm was employed at Doppler shifts corresponding to the ALMA frequency channels, see Section 6.) The horizontal error bar in Figure 6, only $+/-20$ mas, is about 50% larger than the r.m.s. deviation in a linear fit to the 12 main data points. Along the main trend line this implies an r.m.s. error less than 1 km s^{-1}. Of course this applies only to differences among the plotted points, and larger systematic effects may alter the spatial scale. But the main point here is that informal uncertainties of $+/-3$ km s^{-1} are quite reasonable for the Doppler velocities in Table 4.

Clump B?

ACKNOWLEDGMENTS

This paper makes use of the following ALMA data:ADS/JAO.ALMA#2021.1.01054.S and ADS/JAO.ALMA#2013.1.00156.S. ALMA is a partnership of ESO (represent- ing its member states), NSF (USA), and NINS (Japan), together with NRC (Canada) and NSC and ASIAA (Taiwan) and KASI (Republic of Korea), in cooperation with the Republic of Chile. The Joint ALMA Observatory is operated by ESO, AUI/NRAO, and NAOJ. The National Radio Astronomy Observatory is a facility of the National Science Foundation operated under cooperative agreement by Associated Universities, Inc. This research is supported by NSF Grants AST-1907910 and AST-2307305.

REFERENCES

Anugu, N., Baron, F., Gies, D. R. et al. 2023, AJ, 166, 78A

Arroyo-Torres, B., Wittkowski, M., Marcaide, J. M. & Hauschildt, P. H. 2013, A&A, 554, A76

Arroyo-Torres, B., Wittkowski, M., Chiavassa, A. et al. 2015, A&A, 575, A50

Asaki, Y., et al. 2020, ApJS, 247, 23

Choi, Y. K., Hirota, T., Honma, M. et al., 2008, PASJ, 60, 1007

Climent, J. B., Wittkowski, M., Chiavassa, A. et al. A&A, 635, A160

Danchi, W. C, Bester, M., Degiacomi, L. J., & Townes, C. H. 1994, AJ, 107, 1469

Davidson, K. 2020, *Galaxies*, 8, issue 1, 10

Decin, L., Hony, S., de Koter,A. et al. 2006, A&A, 456, 549

Draine, B.T. Physics of the Interstellar Medium, Princeton University Press, pp 248–258.

Eggenberger, P., Ekstrom, S.,Georgy, C. et al. 2021, A&A,, 652,A127

Humphreys, R. M., Davidson, K., Ruch, G., & Wallerstein, G. 2005, AJ, 129, 492

Humphreys, R. M., Helton, L. A., & Jones, T. J. 2007, AJ, 133, 2716

Humphreys, R. M., Ziurys, L. M., Bernal, J. J., et al. 2019, ApJL, 874L, 26H

Humphreys, R. M., Davidson, K., Richards, A.M.S., et al. 2021, AJ, 161, Issue 3 , Id 98

Humphreys, R. M. & Jones, T. J. 2022, AJ, 163, 103H

Jones, T.J., Shenoy, D., & Humphreys, R. M. 2023, RNAAS, 7, 92J

Kaminski, Th. 2019, A&A, 627, 114

Kervella. P., Verhoelst, T., Ridgeway, S.T., Perrin, G., Lacour, S. et al. 2009, A&A, 504, issue 1

Kervella, P., Perrin, G, Chiavassa, A., Ridgeway, S. T., Cami, J., et al. 2011, A&A, 531, A117

Mauron, P. & Josselin, E. 2011, A&A, 526, A156

Montargès, M., Cannon, E., Lagadec, E., et al. 2021, Nature, 594, 365

O'Gorman, E., Vlemmings, W., Richards, A. M. S., et al. 2015, A&A, 573, L1

Richards, A. M. S., Impellizzeri, C. M. V., Humphreys, E. M., et al. 2014, A&A, 572, L9

Richter, L., Kemball, A., & Jonas, J. 2016, MNRAS, 461, 2309

Robinson, L. 1970, Inf. Bull. Var. Stars, 465

Shenoy, D. P., Humphreys, R. M. & Jones, T. J., et al. 2016, AJ, 151, 51

Singh, A. P., Edwards, J. L. & Ziurys, L, M. 2022, AJ, 164, 230

Singh, A. P., Richards, A. M. S., Humphreys, R. M., Decin, L., & Ziurys, L. M, 2023, ApJL, in press

Smartt, S. J. 2015, PASA, 32, e016

Vlemmings, W. H. T., van Langevelde, H. J., & Diamond, P. J. 2002, A &A, 394, 589

Vlemmings, W. H. T., Khouri, T., Mart-Vidal, I. et al. 2017, A&A, 603, 92

Wittkowski, M., Hauschildt, P. H., Arroyo-Torres, B., & Marcaide, J. M. 2012, A&A, 540, L12

Zhang, B., Reid, M. J., Menten, K. M., & Zheng, X. W. 2012, ApJ, 744, 23

Ziurys, L. M., Milam, S. N., Apponi, A. J., & Woolf, N. J. 2007, Nature, 447, 1094